Hindawi
Shock and Vibration
Volume 2022, Article ID 7102702, 19 pages
https://doi.org/10.1155/2022/7102702

Research Article

Numerical Simulation on Dynamic Response of Existing Tunnel to Moving-Axle Loads under the Influence of Oblique Shield Crossing the Intersection Area

Pengcheng Jiang,[1] Mengxi Zhang ,[1] Wurong Jia,[2] Hui Wei,[2] and Akbar A Javadi[3]

[1]*School of Mechanics and Engineering Science, Shanghai University, Shanghai, China*
[2]*Engineering Corporation Limited of China Railway 20th Bureau Group, Kunming, China*
[3]*Department of Engineering, College of Engineering, Mathematics and Physical Sciences, University of Exeter, Exeter EX4 4QF, Devon, UK*

Correspondence should be addressed to Mengxi Zhang; mxzhang@i.shu.edu.cn

Received 30 June 2022; Accepted 3 August 2022; Published 8 September 2022

Academic Editor: Madalina Dumitriu

A 3D dynamic finite element model is developed to study the response of the existing tunnels' concrete structure under the influence of different train speeds and undercrossing with fixed shield excavation. The intersection area of Metro Line 3 in Guangzhou and the intercity railway between Foshan and Dongguan is used as the case study. A programming idea simulating oblique moving-axle loads in the numerical model by using function expressions to constrain activity area is proposed. The Hilber–Hughes–Taylor time-integration scheme is used to calculate the dynamic response parameters of the double-channel rectangular cross section tunnels. Considering fixed excavation steps in the process of shield crossing, acceleration and deformation of the existing tunnels were analyzed under the moving-axle loads of trains at different speeds. From the perspective of the vibration and deformation of existing tunnels, shield excavation and moving speed have their own emphasis on the dynamic influence of the existing tunnel. In addition, the calculation results of the numerical simulation are in good agreement with the data obtained from some field tests, which further verifies the reliability of the calculation method of the numerical model. The results of this research can guide the arrangements for reinforcement measures for existing tunnels in the later stage.

1. Introduction

As important transportation hubs, cities are facing the problem of increasingly tight construction space as the transportation infrastructure continues to improve. With the growing economic and cultural exchange between central cities and neighboring satellite cities, the construction of intercity railways has become a general trend. However, it is not uncommon for new intercity railways to pass through existing underground tunnels in central cities. The existing tunnels may be seriously affected by the environmental disturbance caused by the construction of the new tunnel. Therefore, ensuring the safety and normal use of existing tunnels during the construction of such adjacent tunneling projects is a major challenge [1]. The undercrossing tunneling [2–5] can change the balanced stress field and cause settlement [6], resulting in additional loads and bending moments on the existing structure, which may adversely affect its ordinary operation. Lai et al. [7] used monitoring data and finite difference method (FDM) to study the settlement characteristics of a new shield tunnel passing through an existing tunnel and found that the settlement and torsional deformation of the existing tunnel were the largest at the intersection zone. Chen et al. [8] studied the deformation and stress characteristics of a short-distance EPB shield undercrossing twin tunnels and found that the induced circumferential stress of existing tunnels changed dramatically during the shield crossing. Zhou et al. [9] regarded the existing tunnel as an equivalent rock formation based on the equivalent stratification method and

established a theoretical model for predicting the deformations caused by the construction of a new tunnel undercrossing an existing tunnel based on the Peck formula.

On the other hand, numerical analysis of vibration problems such as wave propagation, structural vibration isolation, and ground vibrations has been widely used in the past few decades [10–15]. Bian et al. [16] conducted full-scale model tests simulating the effects of the moving load of train at multiple speeds and compared the results with the actual field measurements. They showed that the proposed model test could accurately reproduce the dynamic characteristics of the track structure and the foundation soil under the moving load of the train. Shan et al. [17] used a three-dimensional (3D) finite element analysis (FEA) method to simulate shield tunneling activity near a culvert-embankment transition zone and evaluated the impact of shield tunneling on the safety of passing trains by calculating the differential settlement of the transition zone. Nejati et al. [18] simulated ground vibrations caused by train's dynamic load and showed that the most important factors affecting the vibration level of train are axle weight, spacing of axles, and train's speed. During the construction of a new tunnel, in order to ensure the safe operation of the existing high-speed trains, it is necessary to strengthen the new tunnel. The increased rigidity of the reinforced tunnel lining inevitably intensifies the dynamic response of the tunnel lining to the load of the high-speed train [19–21]. The coupled finite element method-boundary element method (FEM-BEM) (where the tunnel structure system is simulated by the finite element method and the soil around the tunnel is simulated by the boundary element method) is widely used in the study of tunnel structure vibration. Jones et al. [22] used FEN-BEM to analyze the influence of tunnel lining on vibration propagation. Using a combination of centrifuge test and numerical simulation, Yang et al. [23] verified that acceptable tunnel characteristics can be obtained when the soil around the tunnel is considered as a homogeneous soil. Huang et al. [24] used two-dimensional and three-dimensional models to numerically simulate the vibration of the train during operation. Their results showed that the acceleration and displacement values obtained by the two-dimensional analysis were much larger than those of the three-dimensional analysis.

A review of the literature shows that there has been a considerable amount of research on the influence of train load on the dynamic response of tunnel structure. However, there has been limited research on the influence of the moving-axle load of the train on the dynamic response of the existing tunnel in combination with the construction disturbance of the newly built tunnel. As the spatial distribution of the surrounding soil layer changes, the impact of the moving-axle load of the train on the dynamic response of the existing tunnel structure is bound to vary, and this directly influences the real-time adjustment of construction measures for new tunnels nearby. Although there have been some experiments that directly applied the train's dynamic load on tunnel tracks and railroad tracks [25], these loads have been applied in the form of cyclic compression on fixed positions of the track in the model. However, this is inconsistent with the reality; as the train moves, it applies dynamic moving-axle load on the track at a particular speed. Therefore, in order to more realistically reflect the response characteristics of tunnel concrete structure to moving trains, it is necessary to apply the load of the train on the track as a dynamic moving-axle load at a certain speed. Also, a large number of research works have been limited to existing tunnels under large intersection angles. Research on shield tunnel passing through the existing tunnel at short distance under small intersection angle is very rare. This paper puts forward a special case, aiming at providing some reference for such problems.

2. Basic Theory

2.1. Dynamic Solution. The nonlinear dynamic response of the structure after the impact of the train is generally solved using the Hilber–Hughes–Taylor (HHT) time-integration method [26], derived from the previous Newmark time-integration method. The implicit HHT format has higher accuracy for any time step Δt. Using the weighted average of the static forces at t and $t+\Delta t$, the equilibrium d'Alambert force, displacement, velocity, and acceleration at time $t+\Delta t$ can be obtained, respectively, by equations (1)–(4):

$$M\{\ddot{u}\}_{t+\Delta t} + (1+n)\{[C]\{\dot{u}\} + [K]\{u\} - P\}_t - \eta\{[C]\{\dot{u}\} + [K]\{u\} - P\}_{t+\Delta t} = 0, \tag{1}$$

$$\{u\}_{t+\Delta t} = \{u\}_t + \Delta t\{\dot{u}\}_t + \Delta t^2\left[\left(\frac{1}{2} - \gamma\right)\{\ddot{u}\}_t + \gamma\{\ddot{u}\}_{t+\Delta t}\right], \tag{2}$$

$$\{\dot{u}\}_{t+\Delta t} = \{\dot{u}\}_t + \Delta t\left[(1-\delta)\{\dot{u}\}_t + \delta\{\ddot{u}\}_{t+\Delta t}\right], \tag{3}$$

$$\{\ddot{u}\}_{t+\Delta t} = \frac{1}{\gamma\Delta t^2}\left[\{u\}_{t+\Delta t} - \{u\}_t\right] - \frac{1}{\gamma\Delta t}\{\dot{u}\}_t - \left(\frac{1}{2\gamma} - 1\right)\{\ddot{u}\}_t, \tag{4}$$

where $[M]$ is the mass matrix, $[C]$ is the damping matrix, $[K]$ is the stiffness matrix, $\{\ddot{u}\}_t$ is the acceleration vector, $\{\dot{u}\}_t$ is the velocity vector, $\{u\}_t$ is the displacement vector, $[P]$ is the load vector, and η is the weighting factor. γ and δ are determined according to η, and the value of η is between 1/3 and 0. When η is equal to 0, the HHT scheme will be simplified to the average acceleration algorithm, the corresponding γ and δ are 0.25 and 0.5, respectively.

Taking a train with six carriages and each carriage has two pairs of wheels at the front and rear as an example, it establishes the nonlinear dynamic motion equations of the train and the structure, respectively. Then combine two equations to obtain the final dynamic equation of the train-structure interaction system, since the equations of motion of the system are the basis for solving the structural deflection expression. Model of 2-axle carriages moving with the same speed over the multi-span continuous beam structure is shown in Figure 1. Motion of the ith carriage is expressed by (5) as follows:

$$M_{vi}\ddot{Y}_i + C_{vi}\dot{Y}_i + K_{vi}Y_i = P_{vi}\,(i = 1, 2, 3, 4, 5, 6), \tag{5}$$

where $Y_i = \{y_{vi}(t), \theta_{vi}(t), y_{1i}(t), y_{2i}(t)\}^T$ is the response vector of the ith carriage, M_{vi}, C_{vi}, and K_{vi} are the mass, damping, and stiffness matrices of the ith carriage, respectively (see). Besides, P_{vi} is the combination of the train-structure interaction force vector and vehicle static load vector expressed by equations 6–(8) as follows:

$$P_{vi} = -\begin{Bmatrix} 0 \\ 0 \\ P_{fi}(t) \\ P_{ri}(t) \end{Bmatrix} + \begin{Bmatrix} 0 \\ 0 \\ \left(\frac{m_{1i} + h_{2i}m_{vi}}{h_i}\right)g \\ \left(\frac{m_{2i} + h_{1i}m_{vi}}{h_i}\right)g \end{Bmatrix}, \tag{6}$$

$$\begin{aligned} P_{fi}(t) &= K_{t1i}\left(y_{1i}(t) - w\left(S_{fi}(t), t\right) - r\left(S_{fi}(t)\right)\right) \\ &\quad + C_{t1i}\left(\dot{y}_{1i}(t) - \dot{w}\left(S_{fi}(t), t\right)\right) + \left(\frac{m_{1i} + h_{2i}m_{vi}}{h_i}\right)g, \end{aligned} \tag{7}$$

$$\begin{aligned} P_{ri}(t) &= K_{t2i}\left(y_{2i}(t) - w\left(S_{ri}(t), t\right) - r\left(S_{ri}(t)\right)\right) \\ &\quad + C_{t2i}\left(\dot{y}_{2i}(t) - \dot{w}\left(S_{ri}(t), t\right)\right) + \left(\frac{m_{2i} + h_{1i}m_{vi}}{h_i}\right)g, \end{aligned} \tag{8}$$

where $r(S(t))$ is the road surface roughness at the location of the corresponding trains' axles. $w(S(t), t)$ and $\dot{w}(S(t), t)$ are the vertical deflection of the train and its time derivative at the location of the corresponding vehicle axles, respectively.

The damping ratio of every vibration mode of structure is assumed to be equivalent. Therefore, the equation of motion of the structure is given by equation (9) as follows:

$$M_{\text{str}}\ddot{U} + C_{\text{str}}\dot{U} + K_{\text{str}}U = H \cdot P_{in}, \tag{9}$$

where U is the structure nodal response vector. M_{str}, $C_{str,}$ and K_{str} are the assembled mass, damping, and stiffness matrices of the structure. H is the global load transformation matrix. In the case of a train system with 2-axle carriages, the transformation matrix H is given in equations (10) and (11):

$$H = \begin{Bmatrix} 0 & \dots & 0 & \dots & 0 & \dots & H_1 & \dots & 0 \\ 0 & \dots & 0 & \dots & H_i & \dots & 0 & \dots & 0 \\ \vdots & \dots & \vdots & \dots & \vdots & \dots & \vdots & \dots & \vdots \\ 0 & \dots & H_6 & \dots & 0 & \dots & 0 & \dots & 0 \end{Bmatrix}, \tag{10}$$

$$H_i = \begin{bmatrix} 0 & \dots & H_{fi}(x,t) \\ H_{ri}(x,t) & \dots & 0 \end{bmatrix}. \tag{11}$$

P_{in} is the interaction force vector containing all interaction forces from every axle. Likewise, in the case of a train system with 2-axle carriages, the interaction force vector P_{in} can be written by (12) as follows:

$$\begin{aligned} P_{in} = \{&P_{f1}(t)P_{r1}(t)P_{f2}(t)P_{r2}(t)P_{f3}(t)P_{r3}(t)P_{f4} \\ &(t)P_{r4}(t)P_{f5}(t)P_{r5}(t)P_{f6}(t)P_{r6}(t)\}. \end{aligned} \tag{12}$$

Combining equations (5) and (9), the train-structure interaction formulation can be obtained, and the equation of motion of train-structure system is given as follows:

$$\begin{aligned} &\begin{bmatrix} M_{\text{str}} & 0 & 0 & 0 \\ 0 & M_{v1} & 0 & 0 \\ 0 & 0 & \ddots & 0 \\ 0 & 0 & 0 & M_{v6} \end{bmatrix} \begin{Bmatrix} \ddot{U} \\ \ddot{Y}_1 \\ \vdots \\ \ddot{Y}_6 \end{Bmatrix} + \begin{bmatrix} C_{\text{str}} + H \cdot C_{tt} \cdot H^T & -H \cdot C_{t1} & \dots & -H \cdot C_{t6} \\ -C_{t1} \cdot H^T & C_{v1} + C_{t1} & \dots & 0 \\ \dots & \dots & \ddots & \vdots \\ -C_{t6} \cdot H^T & 0 & \dots & C_{v6} + C_{t6} \end{bmatrix} \begin{Bmatrix} \dot{U} \\ \dot{Y}_1 \\ \vdots \\ \dot{Y}_2 \end{Bmatrix} \\ &+ \begin{bmatrix} K_{\text{str}} + H \cdot K_{tt} \cdot H^T & -H \cdot K_{t1} \cdot v(t) \cdot \frac{\partial H}{\partial x} \cdot C_{t1} & \dots & -H \cdot K_{t6} \cdot v(t) \cdot \frac{\partial H}{\partial x} \cdot C_{t6} \\ -K_{t1} \cdot H^T & K_{v1} + K_{t1} & \dots & 0 \\ \dots & \dots & \ddots & \vdots \\ -K_{t6} \cdot H^T & 0 & \dots & K_{v6} + K_{t6} \end{bmatrix} \begin{Bmatrix} U \\ Y_1 \\ \vdots \\ Y_2 \end{Bmatrix} = \begin{Bmatrix} -H \cdot K_{tt} \cdot r + H \cdot M_s \\ -K_{t1} \cdot r \\ \vdots \\ -K_{t6} \cdot r \end{Bmatrix}. \end{aligned} \tag{13}$$

The structure is considered as an n-span continuous Euler Bernoulli beam model. Figure 2 presents a finite beam element used in the structure discretization with corresponding nodal degrees of freedom and nodal forces. The shape function of j^{th} element used to transform external acting loads into the nodal load vector can be written by (14) as follows:

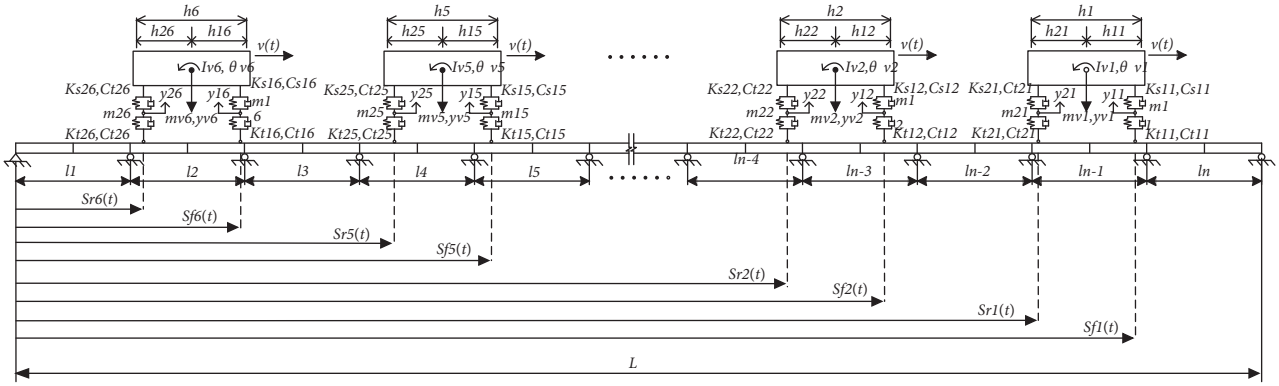

Figure 1: Train-structure system of n-span continuous beam.

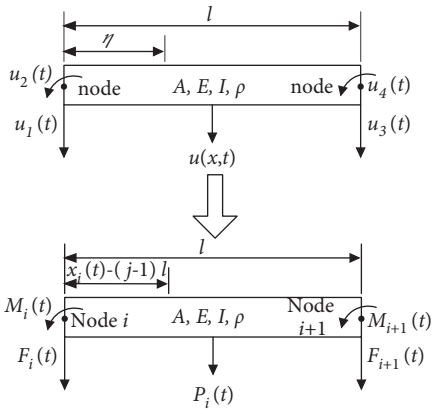

Figure 2: Equivalent nodal loads for the jth element loaded by the train-structure interaction force.

$$H_j(x,t) = \left\{ \begin{array}{c} 1 - 3\left(\dfrac{x_i(t) - (j-1)l}{l}\right)^2 + 2\left(\dfrac{x_i(t) - (j-1)l}{l}\right)^3 \\ x_i(t) - (j-1)l\left(\dfrac{x_i(t) - (j-1)l}{l}\right)^2 \\ 3\left(\dfrac{x_i(t) - (j-1)l}{l}\right)^2 - 2\left(\dfrac{x_i(t) - (j-1)l}{l}\right)^3 \\ x_i(t) - (j-1)l\left(\left(\dfrac{x_i(t) - (j-1)l}{l}\right)^2\right) - \\ \dfrac{((x_i(t) - (j-1)l))^2}{l} \end{array} \right\}. \quad (14)$$

To find the time response of the structure from equation (13), a step-by-step solution can be obtained using the Newmark direct integration method. The deflection of the structure at position x and time t can then be expressed as 1516:

$$w(x,t) = H(x)U(t), \quad (15)$$

$$H(x) = \left\{0 \ldots H(x)_j^T \cdots 0\right\}, \quad (16)$$

where $U(t)$ is the structure nodal response vector at time t, $H(x)$ with $(j-1)l \le x(t) \le$ jl. $H(x)$ is a $1 \times$ NN vector with zero entries except at the degrees-of-freedom corresponding to the nodal displacements of the jth beam element on which the position x is located [27].

2.2. Equation of Motion of Group of Forces Running on Track Deck. With a span length L, constant stiffness EI, constant mass per unit length ρ, and viscous damping ratio C, it considers the time-varying point force $f(x, t)$ moving from left to right at a speed $v(x,t)$ on a simply supported track deck. The track deck is modeled as an Euler beam [28], and the differential equation on the deflection of the beam can be expressed by (17) proposed by Yu and Chan [29] and Chan and Ashebo [30]:

$$\rho\frac{\partial^2 v(x,t)}{\partial t^2} + C\frac{\partial v(x,t)}{\partial t} + EI\frac{\partial v^4(x,t)}{\partial x^4} = f(x,t). \quad (17)$$

With the n^{th} mode shape function of the beam expressed as $\Phi_n(x) = \sin(n\pi x/L)$, the solution of equation (18) is obtained as follows:

$$v(x,t) = \sum_n^{\infty} \Phi_n(x) q_n(t), \quad (18)$$

where n is the number of mode, $q_n(t)$, $(n = 1, 2, \ldots, \square)$ are the n^{th} modal displacements. After substituting equations (18) into (17), integrating the resultant equation with respect to x between 0 and L, and then using the boundary conditions and the properties of the Dirac delta function, the equation of motion in terms of the modal displacement $q_n(t)$ is given by equations (19) and (20) as follows:

$$\frac{d^2q_n(t)}{dt^2} + 2\xi_n\omega_n\frac{dq_n(t)}{dt} + \omega_n^2 q_n = \frac{1}{M}\sum_{k=1}^{N_1}\Phi_n(x_k(t))f(x,t);\ (n = 1, 2, \ldots \infty), \tag{19}$$

$$\omega_n = \frac{n^2\pi^2}{L^2}\sqrt{\frac{EI}{\rho}}; \xi_n = \frac{C}{2\rho\omega_n}, \tag{20}$$

where ω_n, ξ_n are the n^{th} modal frequency, the modal damping ratio, respectively, and M_n is defined as follows:

$$M_n = \int_0^L \rho A\Phi_n^2(x)dx. \tag{21}$$

Considering the group of moving forces, $f(x, t)$ in equation (17) is given by Cebon [31]:

$$f(x,t) = \sum_{k=1}^{N_l}\delta(x - x_k(t))p_k(t), \tag{22}$$

where $x_k(t)$ is the position of the k^{th} force, and $\delta(t)$ is the Dirac delta function.

The response of the system expressed by equation (18) can be solved in the time domain by the convolution integral defined as follows :

$$q_n(t) = \frac{1}{M}\int_0^t h_n(t-\tau)p(\tau)d\tau, \tag{23}$$

where $h_n(t-\tau)$ is the impulse response function and it can be given as follows :

$$h_n(t) = \left(\frac{1}{\omega_n'}\right)e^{-\xi_n\omega_n\Delta t(i-j)}\sin(\omega_n' t);\ t \geq 0, \tag{24}$$

$$\omega_n' = \omega_n\sqrt{1-\xi_n^2}. \tag{25}$$

After substituting equations (24) and (25) into (18) for the generalized coordinate $q_n(t)$, then the dynamic deflection of the beam at point x and time t can be found as follows:

$$v(x,t) = \sum_n^{\infty}\frac{\Phi_n(x)}{M_n}\int_0^t\left(\frac{1}{\omega_n'}\right)e^{-\xi_n\omega_n(t-\tau)}\sin\omega_n'(t-\tau)\sum_{k=1}^{N_l}p_k(t)\Phi_n(x_k(\tau))d\tau. \tag{26}$$

It should be noted that the acceleration of the system can be derived from deflection. Therefore, the acceleration at point x and time t can be obtained as follows:

$$a(x,t) = \frac{\partial^2 v(x,t)}{\partial t^2}, \tag{27}$$

after substituting equations (26) into (27), the owned corresponding equation can be written in discrete terms as follows:

$$a(i) = \frac{1}{M}\sum_{n=1}^{\infty}\Phi_n(x)\left[\Phi_n(c\Delta ti)p(i) + \sum_{j=0}^{i}\ddot{h}(i-j)\Phi_n(c\Delta tj)p(j)\right]. \tag{28}$$

3. Main Components of the System

3.1. Case Study. The Changlong section of the Foshan–Dongguan Intercity Railway starts at Guangzhou South Railway Station and ends at Wanghong Station in Dongguan City. There are 7 stations including Guangzhou South, Changlong, and Panyu Avenue North, with a total length of 36.681 kilometers. This paper takes the Changlong section of the Foshan-Dongguan Intercity Railway under the existing Metro Line 3 tunnel in Guangzhou at the standardized mileage YDK8 + 350~420. The Changlong section of the Foshan-Dongguan Intercity Railway (marked in red in Figure 3) passes under the Metro Line 3 tunnel (marked in green in Figure 3), which forms an intersection area with a small angle of 30°. A typical soil profile in the middle of the intersection area is shown in Figure 4.

3.2. Detailed Introduction of the Numerical Model. The Foshan–Dongguan Intercity Railway Tunnel and Metro Line 3 of Guangzhou in the intersection area are selected as the domain of interest in the numerical model, built in ABAQUS. The Foshan–Dongguan Intercity Railway Tunnel is a shield tunnel and Metro Line 3 is an existing tunnel in the intersection area. The entire domain of the numerical model is discretized into 263553 elements. Except for the existing tunnel for which the element type C3D4 is used, the element type of all other components is C3D8. The whole three-dimensional model shown in Figure 5 is 112 m long, 120 m wide in the cross-sectional direction of the shield tunnel, and 52.3 m deep. The newly built shield tunnel has a buried depth of 24.9 m and is divided into two lines on the left and right. According to the sequence of construction, the left-line shield machine first will pass through the existing tunnel (as shown in Figure 5), and after the left-line shield machine completed the excavation process for a total of 70 rings, the right-line shield machine will cross through the soil layers below the existing tunnel with a buried depth of 8 m. The angle between the existing tunnel and the shield tunnel is 30°, hence the length of the existing tunnel in the numerical model is about 129.3 m. The existing tunnel with specific geometric dimensions shown in Figure 5 is composed of a single-layer double-span structure and single-layer single-span structures. The numerical model simulates static

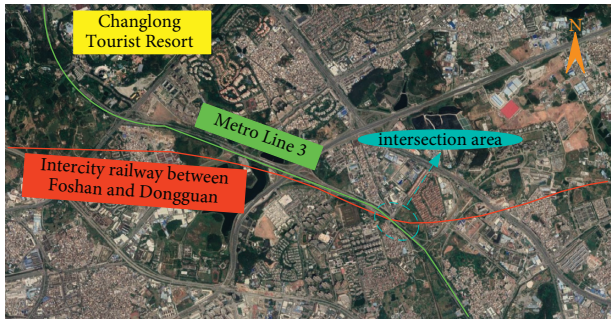

Figure 3: Plan view of project site.

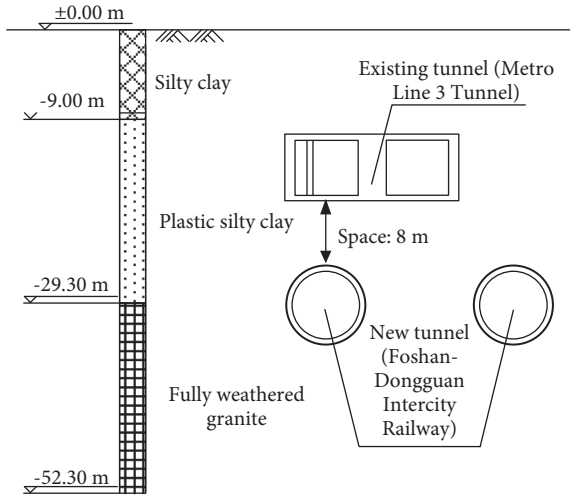

Figure 4: Typical soil profile in the middle of intersection area.

excavation before applying dynamic loads. Before the excavation of the soil layer, the existing tunnel and the whole soil layers are involved in the stress cancellation to eliminate the original settlement caused by gravity. In the design part of the numerical model, the methods interpreted as suppressing soil elements at the excavation site and activating the lining elements and grouting elements are used to simulate the shield excavation process. The equivalent layer elements used to replace the slurry and over-excavated voids are activated to simulate the construction process of grouting and exerting segments during the shield excavation. During the entire crossing process, the left-line shield machine first traverses the single-layer double-span section of the existing tunnel, and then traverses the single-layer single-span section, while the right-line shield machine always passes through the single-layer single-span sections of the existing tunnel in sequence. The two shield machines on the left and the right need to go through 70 rings to complete the penetration of the entire three-dimensional soil layers. A number of special cases (marked in Figure 5), interpreted as shield machines reaching different positions (including the left line reaching to the 15th ring, the left line to the 30th ring, the left line to the 44th ring, the right line to the 38th ring, the right line to the 52th ring, and the right line to the 67th ring), are selected as the working condition for comparative study. Finally, when the shield machine advances to the set excavation position, moving-axle loads with different speeds are applied to run on the rails of the existing tunnel to simulate dynamic loading. Reflection and refraction will occur when the dynamic load propagates to the boundary position due to the limited size of the numerical model, which will cause certain errors in the calculation results. Moreover, this model simulates the semi-infinite field of the overall model by setting up the artificial boundary [32], which better solves the reflection and refraction problems of the dynamic load propagating to the boundary. The artificial boundary, which is shown in Figure 5, is specifically set at the periphery and bottom boundary of the 3D numerical model.

The damping matrix of the system adopts Rayleigh damping [33], and the specific expressions are shown as

$$[C] = \alpha[M] + \beta[K], \tag{29}$$

$$\begin{cases} \alpha = \dfrac{2\omega_i\omega_j}{\omega_i + \omega_j}\xi, \\ \beta = \dfrac{2}{\omega_i + \omega_j}\xi, \end{cases} \tag{30}$$

where α and β are the Rayleigh damping coefficients, ω_i and ω_j are generally the first two modes of the system, and ξ is the damping ratio of the soil. The three-dimensional viscoelastic artificial boundary is processed by an equivalent spring-damper system [32], and the corresponding tangential and normal spring stiffness and damping coefficients are taken according to the following formulas shown as:

$$K_{BT} = \alpha_T \frac{G}{R}, C_{BT} = \rho c_s, \tag{31}$$

$$K_{BN} = \alpha_N \frac{G}{R}, C_{BN} = \rho c_p, \tag{32}$$

where K_{BN} and K_{BT} are the spring normal and tangential stiffness, respectively; C_{BN} and C_{BT} are the damping coefficients of the damper in the normal and tangential directions, respectively; R is the distance from the wave source to the artificial boundary point; c_s and c_p are, respectively, S and P velocities of wave; G is the medium shear modulus; ρ is the mass density of the medium; α_T and α_N are the correction coefficients of the tangential and normal viscoelastic artificial boundary.

3.3. Material Characteristics. Based on the borehole data, the actual site is simplified to horizontal layered soil layers to achieve more effective grid division. The soil in the numerical model is divided into three layers including silty clay, plastic silty clay, and fully weathered granite. The Mohr–Coulomb constitutive model with damping is used to simulate the stress-strain relationship of the soil under dynamic loading. The mechanical parameters of soil are given in Table 1. The EPB-TBM shield with the ignored conicity [34] has a cylindrical shape [35]. Specific parameters for the shield body are listed in Table 2. In the construction

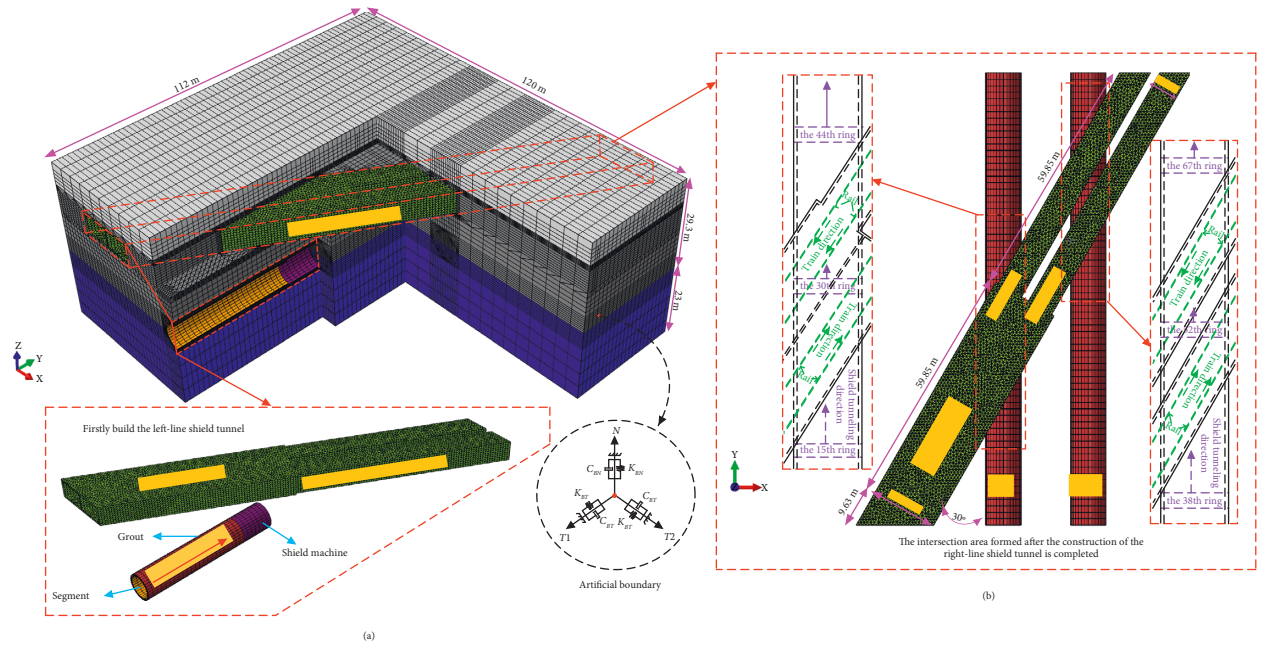

Figure 5: 3D finite element numerical model: (a) location relationship between the left-line shield tunnel and metro line 3 tunnel; (b) labeling of specific detailed construction steps for shield tunneling through intersection area.

of the shield tunnel of the Foshan–Dongguan Intercity Railway, the over-excavated space generated by the shield machine is filled with grout, and the numerical model uses an equivalent circular concrete layer with the inner radius of 4.25 m to fill the gap. Considering that the hardening of the concrete grout is accompanied by the process of shield tunneling, the elastic modulus of the concrete layer is set to 0.58 MPa, 6.8 MPa, and 23 MPa in three stages. In the first stage, the initial setting stage of the grout is around the latest laid three pipe rings, and the initial elastic modulus is 0.58 MPa. In the second stage, the solidification of the grout occurs in the intermediate stage at the latest laid 4^{th} to 6^{th} pipe rings, and the equivalent elastic modulus is 6.8 MPa. The equivalent elastic modulus of the filling grout at the other completed pipe rings is set to 23 MPa. The specific material parameters of the three types of grout following a sequence are given in Table 3. Similarly, the parameters of the segmental lining with inner radius of 3.85 m are included in the newly built shield tunnel, and the parameters of the existing tunnel are summarized in Table 3. Before applying the moving-axle load of the train, the three-dimensional soil layers need to be excavated in a static state. According to the buried depth of the shield tunnel and the setting specifications of the excavation parameters in the construction plan, the thrust of the excavation face and the grouting pressure of the shield tunneling are set to 0.17 MPa and 0.5 MPa, respectively.

4. Introduction of Moving-Axle Loads

To analyze the effects of the load imposed by train on the tunnel structure, this paper considers the use of vertical excitation force to simulate the moving-axle loads [36]. The moving-axle load of the train is simulated by the artificial excitation force function proposed based on the theoretical research and test data of the British Railway Technology Center. The part of the wheel/rail force below 5 Hz is mainly produced by the relative motion of the car body to the suspension part. The intermediate frequency component of 30~60 Hz reflects the rebound effect of the wheel relative to the rail, and the high-frequency component of 200~400 Hz is produced by the movement of the rail by the resistance of the wheel-rail contact surface. The artificial excitation force function used to simulate the vertical load of the train is composed of the static load of the train wheels and the dynamic load formed by a series of sine functions, which are shown as:

$$F(t) = P_0 + P_1 \sin(\omega_1 t) + P_2 \sin(\omega_2 t) + P_3 \sin(\omega_3 t), \quad (33)$$

$$P_i = M_0 \alpha_i \omega_i^2 \qquad \omega_i = \frac{2\pi v}{L_i} \quad (i = 1, 2, 3), \quad (34)$$

where P_0 is the static load of a single wheel, and the weight of the running train in this model determines the value of P_0 as 84.75 kN; P_1, P_2, and P_3, respectively, represent the typical values of the vibration load defined by the additional dynamic load acting on the line and the wear of the rail surface according to the driving comfort; ω_i is the circular frequency of the irregular vibration wavelength corresponding to the train speed v; M_0 is the mass under spring of the train, the mass under spring of each train in this model is 1770 kg; α_i is typical vector height; L_i is typical wavelength; the values of α_1 and L_1 corresponding to P_1 are 3.5 mm and 10 m; the values of α_2 and L_2 corresponding to P_2 are 0.4 mm and 2 m, and the values of α_3 and L_3 corresponding to P_3 are 0.08 mm and

Table 1: Mechanical parameters of soil layers in the numerical model.

Type of soil layer	Density (kg/m^3)	Elastic modulus (MPa)	Poisson ratio	Friction angle (o)	Cohesion (kPa)
Silty clay	1820	10.33	0.33	7	12
Plastic silty clay	1850	15.32	0.31	17.03	19.4
Fully weathered granite	1960	21.97	0.29	21.3	18.17

Table 2: Geometry and material parameters of shield machine.

Diameter of the cylinder shape (m)	Length (m)	Thickness (m)	Density (kg/m^3)	Elastic modulus (GPa)	Poisson ratio
8.8	11.2	0.2	3000	2080	0.2

Table 3: Material parameters of various types of concrete.

Location	Length (m)	Thickness (m)	Density (kg/m^3)	Elastic modulus (MPa)	Poisson ratio
Grouting layer (1)	1.6	0.15	2068	0.58	0.31
Grouting layer (2)	1.6	0.15	2163	6.8	0.27
Grouting layer (3)	1.6	0.15	2260	23	0.21
Segmental lining	1.6	0.4	2350	33600	0.23
Existing tunnel	—	0.7	2500	30240	0.2

0.5 m. The different dynamic responses of the existing tunnel in the intersection area will be triggered by the train in the existing tunnel passing through the intersection area at different speeds of 50 km/h, 75 km/h, 100 km/h, and 125 km/h. Corresponding to these four speeds, the times required for the train to completely pass through the entire model domain are 19.16 s, 12.78 s, 9.58 s, and 7.66 s, respectively. A method, shown in the form of a flowchart in Figure 6, is adopted to compile the moving-axle load of the train into a set of procedures, which can be readily implemented in ABAQUS.

Furthermore, to illustrate the action area and action form of the moving-axle load of the two trains, A and B, running on the rails in the existing tunnel, Figure 7 shows the details of the load of the first carriage of each train. Based on the premise of the implicit integration calculation method and that the time step should not be exceeding 1/100 of the maximum natural period, the step size of the total integration time is set to 0.01 seconds.

5. Observation Points on Existing Tunnel

The dynamic response of the existing tunnel structure with trains running opposite to each other in it is the core of the numerical calculation task. Relevant research results [37] show that the only center position of each cross section on the track bed is the most typical representative of the dynamic response of the structure under the external load. In addition, for the on-site measurement scheme of existing tunnels, the only center position of each cross section on the track bed is also selected as the installation position of the measuring instrument. Figure 8 shows the detailed position information of each observation point on the center of the existing tunnel. It is seen that the single-layer double-span section and the single-layer single-span section of the existing tunnel are connected to each other in Figure 8. The 1st observation point of each cross section constitutes the set of observation points on the left track bed of the existing tunnel, while the 6th observation point of each cross section constitutes the set of observation points on the right track bed of the existing tunnel. Each line has 49 cross sections in total, and the 1st and the 6th observation points of each section are located in the middle of the concrete slab under the two-track beds. The observation points located in the intersection area on the existing tunnel are marked in red in Figure 8.

6. Emphasis of Research Content

Based on the difference in the process of excavation in the intersection area and the difference in the speed of the train running in the existing tunnel, extracting and analyzing the characteristics of peak acceleration and peak displacement on each observation point along the running direction of the train is the focus of the investigation of the dynamic disturbance to the existing tunnel. Although the newly built shield tunnel under the existing tunnel crosses the intersection area in the order of construction, the actual time required for the shield machine excavating a ring is much longer than the time for the train passing through the whole length of the existing tunnel. As a result, there is a significant difference in the dynamic disturbance to the concrete structure of the existing tunnel caused by the moving train.

7. Results and Discussion

7.1. Peak Acceleration along the Track Bed of the Existing Tunnel. According to the construction sequence of the newly built tunnel, the right-line shield machine passes through the intersection area after the left-line shield machine has run through the overall model. Figure 9 shows the distribution of peak acceleration along the bottom floor of the existing tunnel when the left-line shield machine reached the 15th ring, the 30th ring, and the 44th ring in sequence. Figure 10 shows the distribution of peak acceleration along the bottom floor of the existing tunnel when the right-line

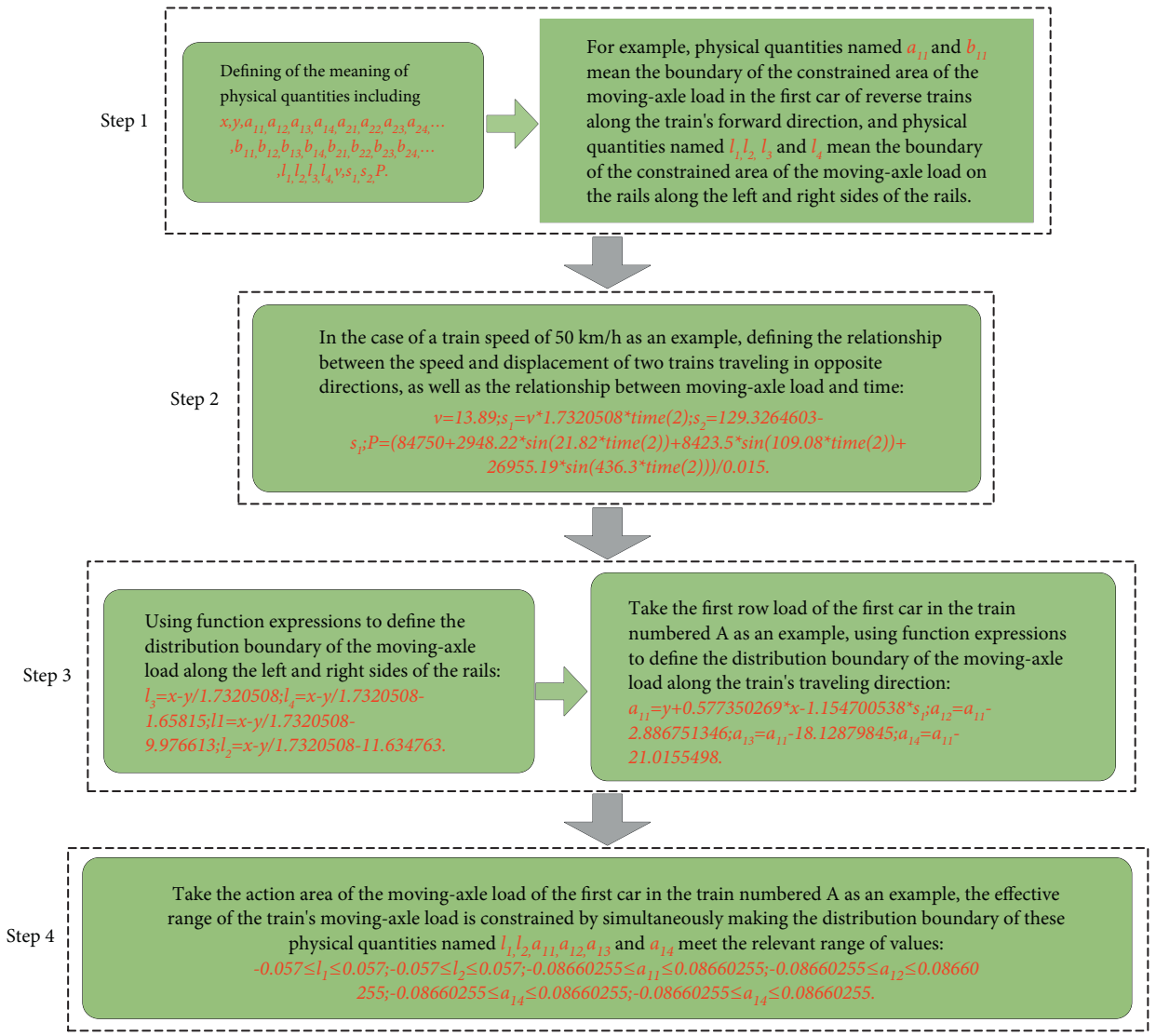

Figure 6: The main steps of using formula translation to edit the subroutine of the train's moving-axle load.

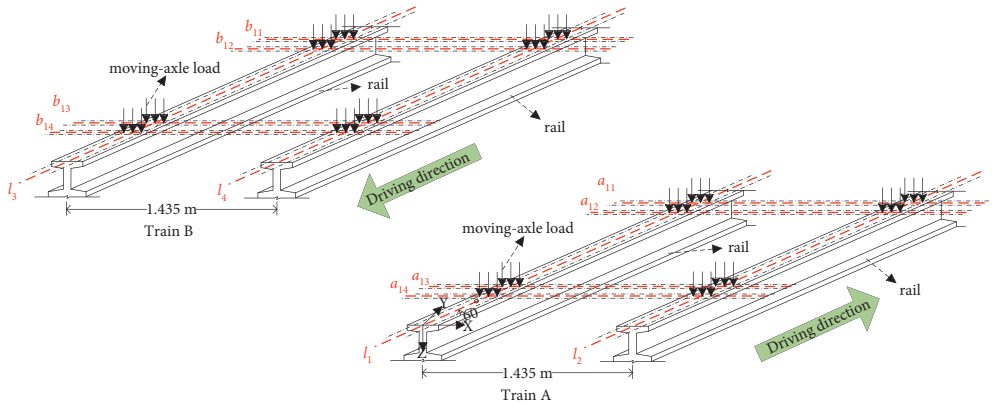

Figure 7: Schematic diagram of the constrained area of the first carriage with moving-axle loads on rails.

shield machine successively arrived at the 38th, 52th, and 67th rings. It is seen that when the speed of train increases from 50 km/h to 125 km/h, the peak acceleration of the observation points along the left and right bottom floors of the existing tunnel also increases. When the left-line shield machine advances to the 15th ring, which is about to enter

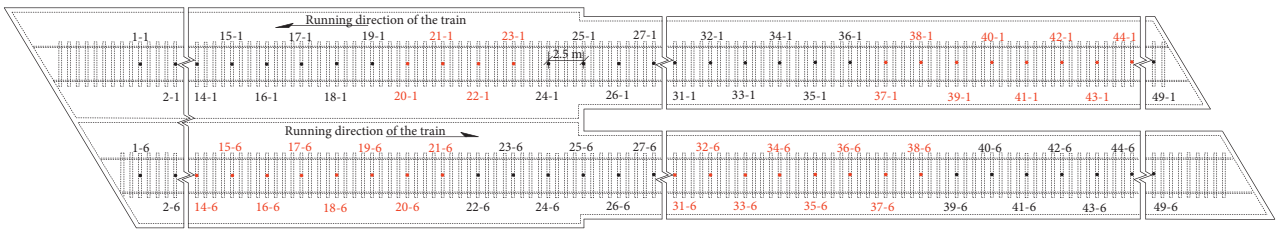

Figure 8: Observation points on the track beds of metro line 3 tunnel.

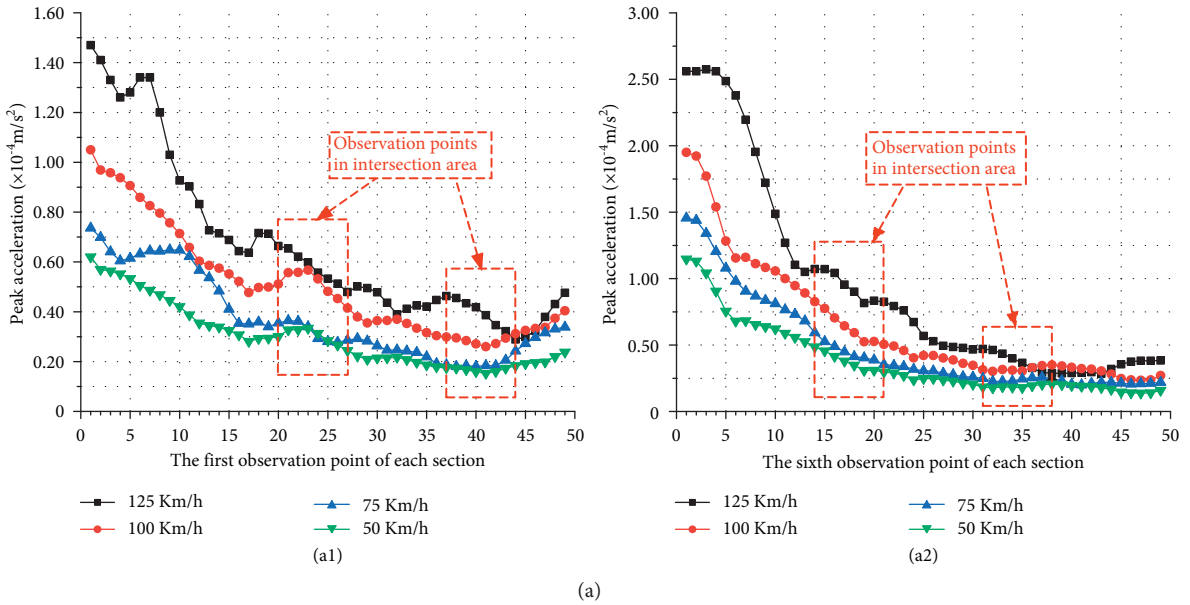

(a)

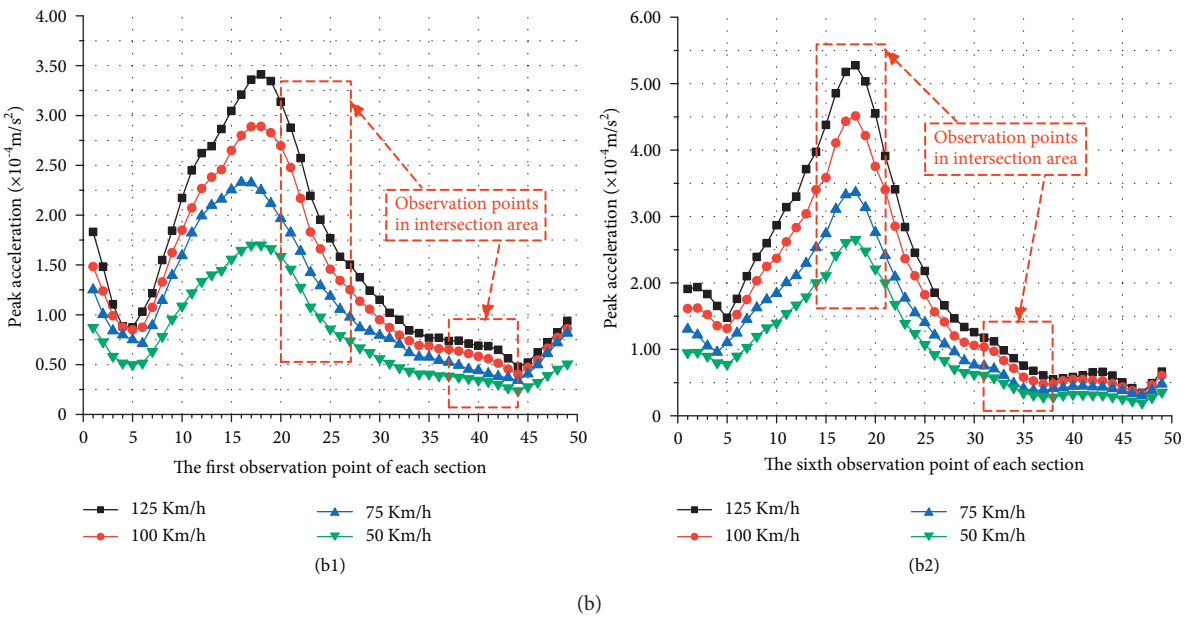

(b)

Figure 9: Continued.

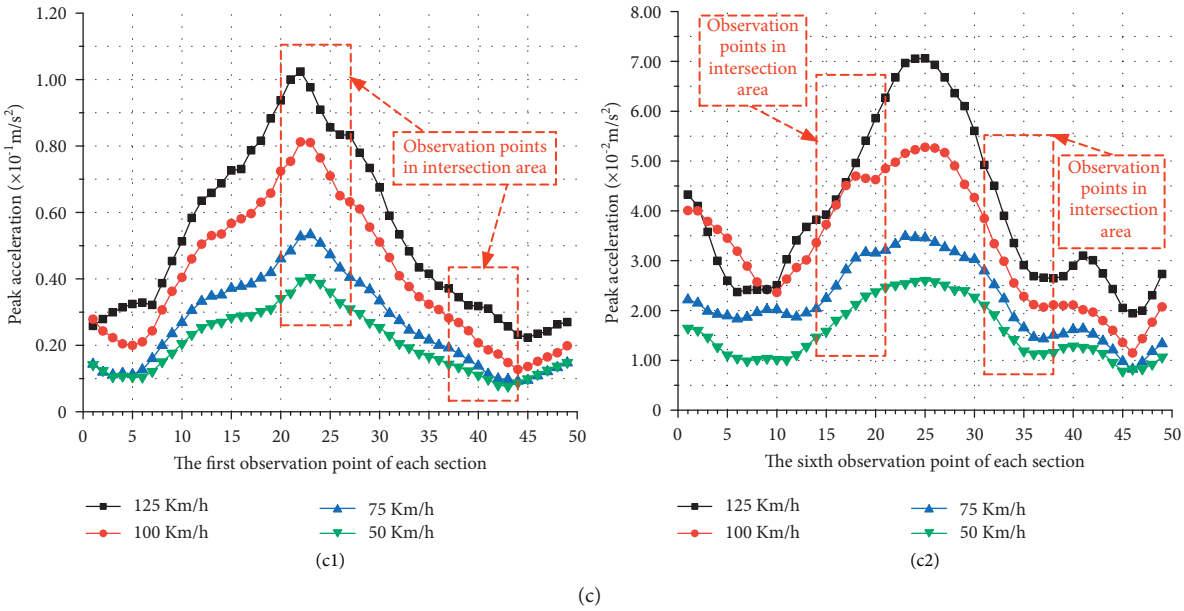

FIGURE 9: Peak acceleration of observation points on the existing tunnel: (a) shield excavation reaches the 15th ring on the left; (b) shield excavation reaches the 30th ring on the left; and (c) shield excavation reaches the 44th ring on the left.

the intersection area, the peak acceleration of the observation points along the bottom floor of the existing tunnel shows an overall decreasing trend. But the peak acceleration along the right bottom floor of the existing tunnel (the sixth observation point of each section) is generally higher than along the left side (the first observation point of each section). Next, when the left-line shield machine advances to the 30th ring which has passed through the single-layer double-span section on the right of the existing tunnel, as the trains move in the existing tunnel at the same speed, it is seen that the maximum peak acceleration along the right floor of the existing tunnel (the sixth observation point of each section) appears within the intersection area (the 18th section of the existing tunnel itself). Also, the peak acceleration along the right floor of the existing tunnel (the sixth observation point of each section) is still generally higher than along the left side (the first observation point of each section). As the left-line shield machine reaches the 44th ring with the continuous excavation, the peak acceleration along the left floor of the existing tunnel is in turn higher than that along the right floor. Considering the changes in train's speeds (50 km/h, 75 km/h, 100 km/h, and 125 km/h), the corresponding maximum values of peak accelerations of the left floor of the existing tunnel appear on the 23rd section (0.04 m/s^2), the 23rd section (0.053 m/s^2), the 22nd section (0.081 m/s^2), and the 22nd section (0.102 m/s^2), respectively. At the same time, the maximum values of peak acceleration of the right floor on the existing tunnel corresponding to these four speeds appear on the 25th section (0.026 m/s^2), the 23rd section (0.035 m/s^2), the 25th section (0.053 m/s^2), and the 25th section (0.071 m/s^2), respectively.

Considering the changes in the specific position of the maximum peak acceleration on the existing structure under different working conditions, it can be concluded that the change in vibration of the existing structure under the action of the train's moving-axle load is clearly affected by the disturbance of the undercrossing new shield tunnel. It should be noted that the 25th cross section is the interface between the single-layer double-span section and the single-layer single-span section of the existing tunnel. The existing structure here has solidified due to the geometric properties of the cross-sections, hence the 25th cross section is the most vulnerable part of the entire existing structure. Therefore, the closer the position on the structure is to the interface, the higher the degree of vibration caused by the dynamic load. As the right-line shield machine starts to enter the intersection area, the characteristic is that the position appearing the maximum value of peak acceleration along the left and right sides of the existing tunnel continuously moves to the right direction unanimously in Figures 9 and 10, which is consistent with the right-shifting of the position on the cross section appearing the maximum value of peak acceleration during the whole process of the left-line shield machine passing through the intersection area. Moreover, compared with the case where the maximum value of the peak acceleration curve along the left-side structure on the existing tunnel continuously shifts to the right, the maximum value of the curve along the right-side on the existing tunnel moves faster with no transformation throughout the entire process of the shield machine traversing the intersection area. This shows that the various parts along the right-side of the existing tunnel which are passed through first by the shield machine are more sensitive to the change in the dynamic response to the train's moving-axle load. The characteristics obtained from the above analysis fully indicate that the speed of subway trains running in both the left and right directions in the existing tunnel, should be adjusted flexibly according to the specific conditions of the

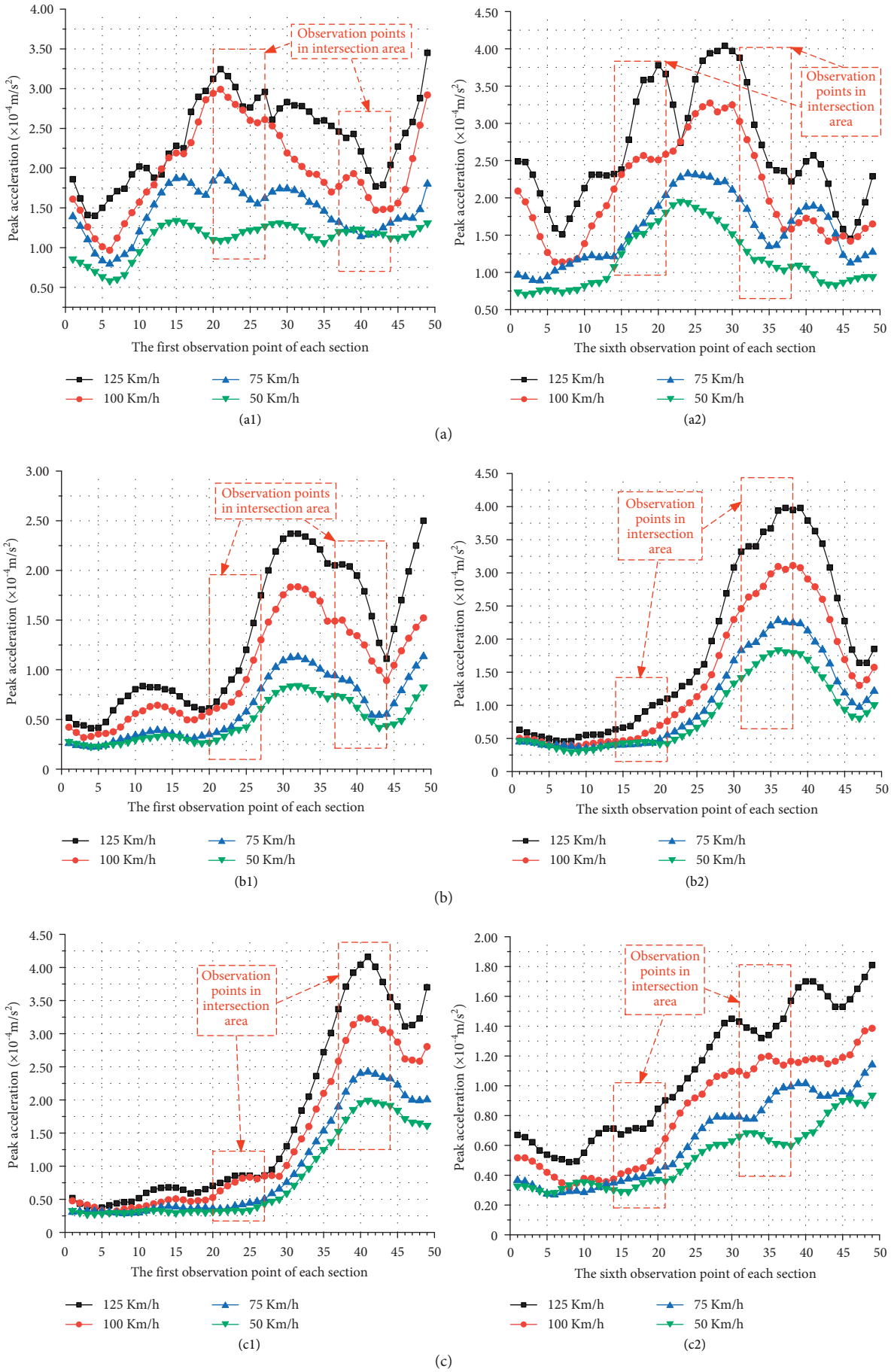

Figure 10: Peak acceleration of observation points on existing tunnel: (a) shield excavation reaches the 38th ring on the right; (b) shield excavation reaches the 52th ring on the right; and (c) shield excavation reaches the 67th ring on the right.

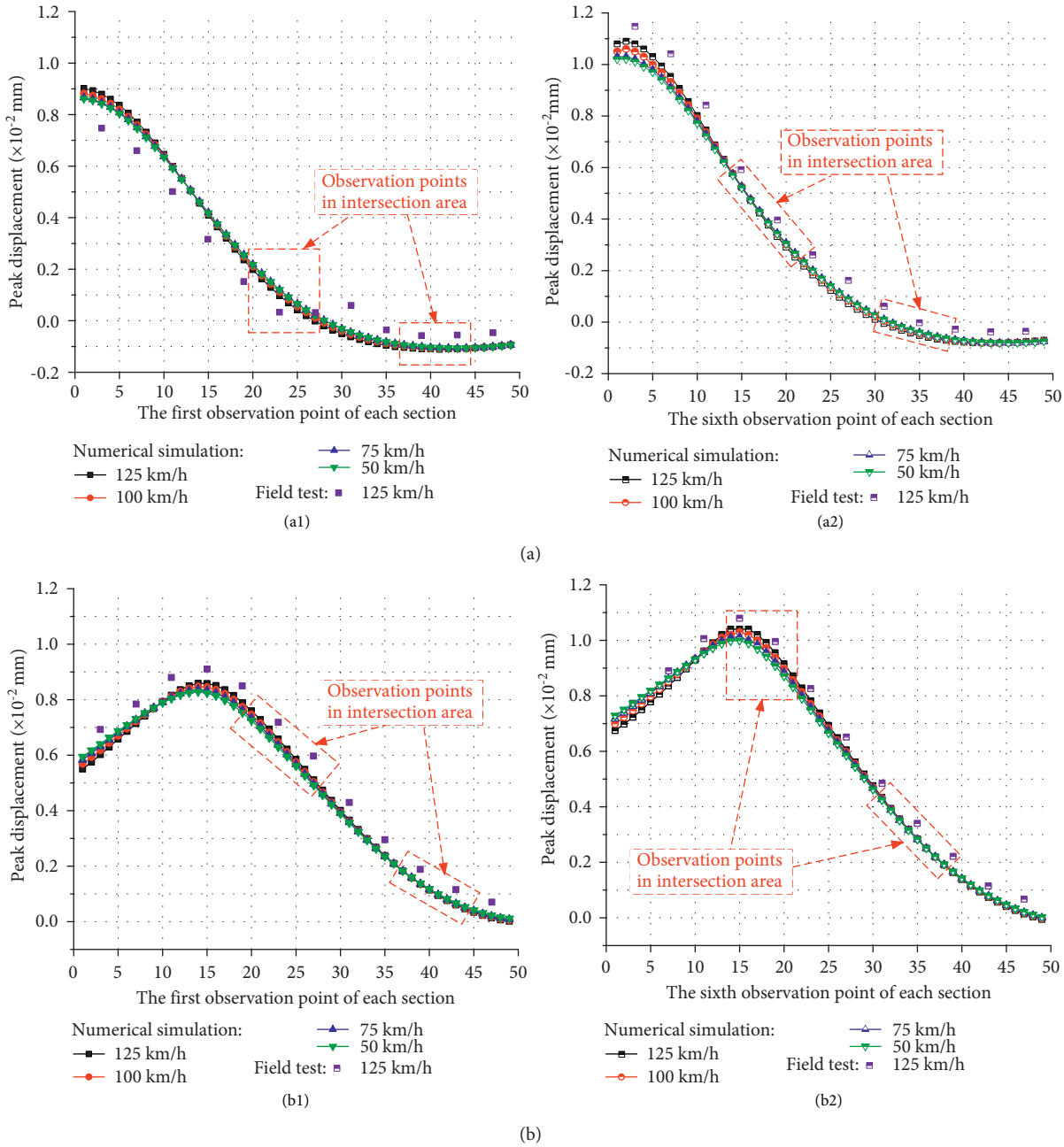

Figure 11: Continued.

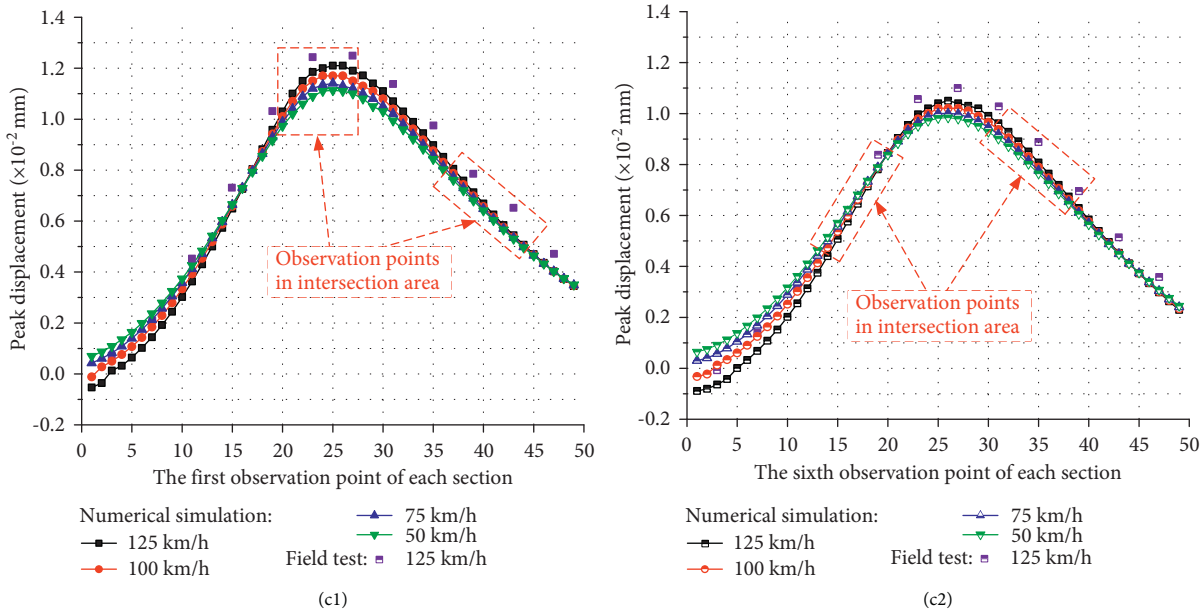

(c)

Figure 11: Peak displacement of observation points on existing tunnel: (a) shield excavation reaches the 15th ring on the left; (b) shield excavation reaches the 30th ring on the left; (c) shield excavation reaches the 52th ring on the left.

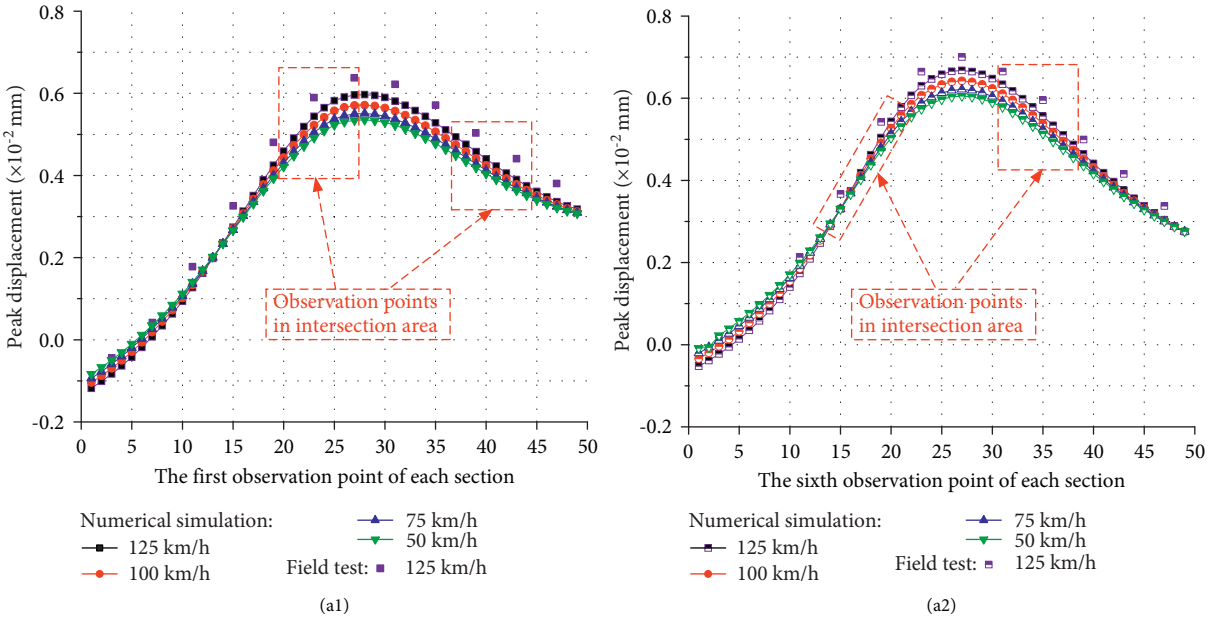

(a)

Figure 12: Continued.

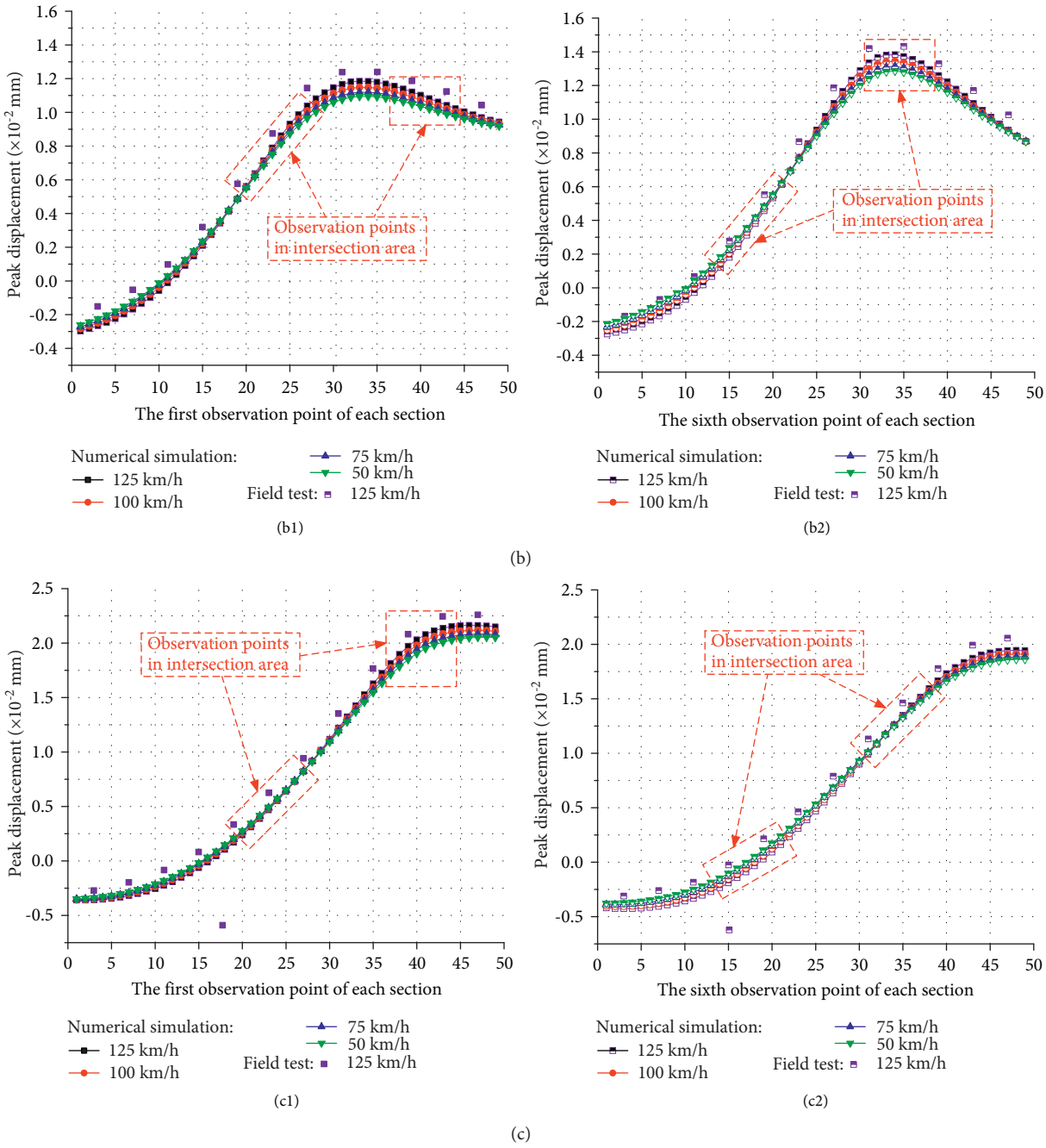

Figure 12: Peak displacement of observation points on existing tunnel: (a) shield excavation reaches the 38th ring on the right; (b) shield excavation reaches the 52th ring on the right; (c) shield excavation reaches the 67th ring on the right.

undercrossing construction. This can minimize the difference in the dynamic response of the left and right slabs of the existing tunnel to the train's moving-axle load.

7.2. Peak Displacement along the Track Bed of the Existing Tunnel. The vibrational displacement of the track beds on the concrete structure of the existing tunnel under the action of train's moving-axle load is directly related to the stability of the running train. Figures 11 and 12, respectively, summarize the values of peak displacements of the 1st and 6th observation points on each cross section on the existing tunnel when the left-line and right-line shield machines reach typical locations in the intersection area. In order to accurately observe the peak displacements of the observation points on the existing tunnel track beds located in the intersection area, the corresponding observation points are enlarged in the figures and the values of the individual points are selectively labeled. Based on the results, the difference in the values of peak displacements of the observation points on the track beds is very small with the trains running at four different speeds. This is because the moving-axle load

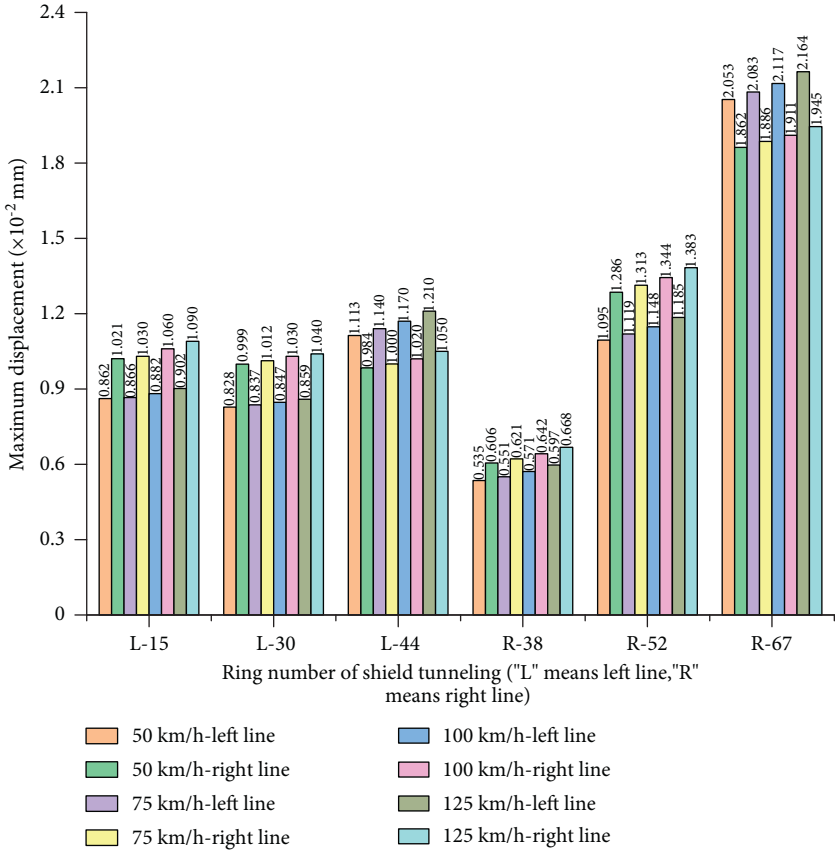

Figure 13: The maximum value of the peak displacement of the observation points on the track beds of the existing tunnel.

applied by the moving subway train does not cause significant deformation on the concrete structures with a certain embedded depth and high level of rigidity. With the excavation of the shield machine, the position of the observation point on specific cross section where the maximum value of peak displacement is located continues to move to the right in Figures 11 and 12, the maximum value of peak displacement along the track beds of the existing tunnel increases constantly with the continuous excavation of the shield machine. In addition, after the right-line shield machine completes the crossing of the intersection area, the maximum value of peak displacement along the track beds of the entire length of the existing tunnel reaches a new level. It can be observed that when the left-line shield machine reaches the 15th and the right-line machine latterly arrives at the later 38th rings, the peak displacement along the right side of the existing tunnel is generally higher than that on the left side with the soil layer in intersection area under the left side of the existing tunnel never being excavated. Similarly, when the left-line shield machine reaches the 44th ring and the right-line shield machine reaches the 67th ring later, the trend of distribution of the peak displacement reverses; the peak displacement along the left side of the existing tunnel becomes higher than the right side. In other words, which side of the existing tunnel has a higher peak displacement is determined by which side is traversed first by the new shield tunnel. The maximum values of the peak displacement along the left and right track beds of the existing tunnel are shown in Figure 13. Corresponding to the speed including 50 km/h, 75 km/h, 100 km/h, and 125 km/h, the left-line shield machine advancing to the 44th ring compared with it advancing to the 15th ring makes the maximum value of peak displacement of the left track bed on the existing tunnel increased, respectively, by 29.2%, 31.6%, 32.7%, and 34.1%, as well as makes the corresponding maximum value of the right track bed on the existing tunnel increased by −3.6%, −2.91%, −3.77%, and −3.67%, respectively. Subsequently, corresponding to the speed of the train in turn similarly, the right-line shield machine advancing to the 67th ring compared with it advancing to the 38th ring makes the maximum value of peak displacement of the left track bed on the existing tunnel increased respectively by 283.5%, 278.3%, 270.6%, and 262.4%, and makes the corresponding maximum value of the right track bed on the existing tunnel increased by 207.6%, 203.5%, 197.5%, and 191.3%, respectively. From the perspective of the increase in the maximum displacement, whether the shield machine on the left-line or the right-line crosses the intersection area, the increase in maximum displacement along the left track bed of the existing tunnel is higher than that of the right side and the maximum value also increases with increasing the train's speed. Lastly, it should be emphasized that the intersection area, including the existing tunnel and the shield tunnel, is truly formed after the left side of the existing tunnel completely traverses in the later

period. This is why a more significant increment in the maximum value of the peak displacement occurred along the left side of the existing tunnel. Therefore, the sequence of the shield machine crossing the left and right sides of the existing tunnel has a significant impact on the deformation of the existing tunnel.

8. Conclusions

This paper presented a three-dimensional dynamic finite element model to study the dynamic response of existing tunnels under the influence of different train speeds and undercrossing with fixed shield excavation. The model has been applied to a real case study involving the intersection area of Metro Line 3 in Guangzhou and the intercity railway between Foshan and Dongguan in China. By running the edited program into the three-dimensional finite element calculation model, the effect of running moving-axle loads at different speeds on the rails of the existing tunnel is realized. It has calculated and analyzed the peak acceleration and peak displacement of the existing tunnel. The curves of the dynamic values of the existing tunnel are compared from different analytical perspectives, and the difference in the dynamic characteristic of the existing tunnel under different working conditions is studied. The following conclusions are drawn from the results:

(1) The speed of the train significantly affects the peak acceleration of the existing tunnel. As the speed of the train increases, the overall response acceleration of the existing tunnel also increases. However, the peak displacement of the existing tunnel is generally insensitive to the influence of the moving-axle load imposed by train under different speeds. With the continuous excavation of new shield tunnels, the locations where the maximum values of peak acceleration and peak displacement of the existing tunnels occur show a tendency to continuously moving along the longitudinal direction of the concrete structure itself. The value of peak acceleration of the existing tunnel as a whole reaches the highest level when the newly built shield tunnel reaches the vicinity of the cross section in the middle of the existing tunnel. However, the overall peak displacement of the existing tunnels continues to increase with the continuous advancement of the newly built shield tunnels on the left and right lines.

(2) The rising amplitude of the peak displacement on the left and right sides of the existing tunnel caused by the crossing process of the left-line shield is obviously lower than that caused by the right-line shield. Besides the impact of shield tunneling on the peak displacement of the existing tunnel is manifested more in the subsequent construction process of the shield tunnel on the right line. By the way, which side of the existing tunnel has a more significant dynamic response depends on the specific position reached by the undercrossing shield.

(3) In the next phase of this research work, the effects of change in the excavation intervals of the left and right shields will be investigated. The research work will focus on the difference in the dynamic response of existing tunnels to the moving-axle loads at established speeds when the left and right shields pass through the intersection area at different intervals.

Appendix

$$M_{vi}=\begin{Bmatrix} m_{vi} & 0 & 0 & 0 \\ 0 & I_{vi} & 0 & 0 \\ 0 & 0 & m_{1i} & 0 \\ 0 & 0 & 0 & m_{2i} \end{Bmatrix}; M_s=\begin{Bmatrix} \dfrac{(m_{11}+h_{21}m_{v1})}{h_1}g \\ \dfrac{(m_{21}+h_{11}m_{v1})}{h_1}g \\ \dfrac{(m_{12}+h_{22}m_{v2})}{h_2}g \\ \dfrac{(m_{22}+h_{12}m_{v2})}{h_2}g \end{Bmatrix}; C_{vi}=\begin{bmatrix} C_{s1i}+C_{s2i} & -C_{s1i}h_{1i}+C_{s2i}h_{2i} & -C_{s1i} & -C_{s2i} \\ -C_{s1i}h_{1i}+C_{s2i}h_{2i} & -C_{s1i}h_{1i}^2h_i+C_{s2i}h_{2i}^2h_i & C_{s1i}h_{1i} & -C_{s2i}h_{2i} \\ -C_{s1i} & C_{s1i}h_{1i} & C_{s1i} & 0 \\ -C_{s2i} & -C_{s2i}h_{2i} & 0 & C_{s2i} \end{bmatrix},$$

$$K_{vi}=\begin{bmatrix} K_{s1i}+K_{s2i} & -K_{s1i}h_{1i}+K_{s2i}h_{2i} & -K_{s1i} & -K_{s2i} \\ -K_{s1i}h_{1i}+K_{s2i}h_{2i} & -K_{s1i}h_{1i}^2h_i+K_{s2i}h_{2i}^2h_i & K_{s1i}h_{1i} & -K_{s2i}h_{2i} \\ -K_{s1i} & K_{s1i}h_{1i} & K_{s1i} & 0 \\ -K_{s2i} & -K_{s2i}h_{2i} & 0 & K_{s2i} \end{bmatrix}; C_{ti}=\begin{bmatrix} 0 & 0 & 0 & 0 \\ 0 & 0 & 0 & 0 \\ 0 & 0 & C_{1ti} & 0 \\ 0 & 0 & 0 & C_{12i} \end{bmatrix}; K_{ti}=\begin{bmatrix} 0 & 0 & 0 & 0 \\ 0 & 0 & 0 & 0 \\ 0 & 0 & K_{1ti} & 0 \\ 0 & 0 & 0 & K_{12i} \end{bmatrix}, \tag{A1}$$

$$C_{tt}=\begin{bmatrix} C_{t1} & 0 \\ 0 & C_{t2} \end{bmatrix}; K_{tt}=\begin{bmatrix} K_{t1} & 0 \\ 0 & K_{t2} \end{bmatrix}; r=\begin{Bmatrix} r\left(x_{f1}(t)\right) \\ r\left(x_{r1}(t)\right) \\ r\left(x_{f2}(t)\right) \\ r\left(x_{r1}(t)\right) \end{Bmatrix}.$$

Data Availability

The data used to support the findings of the study are included within this article.

Conflicts of Interest

The authors declare that they have no conflicts of interest.

Acknowledgments

This research work was financially supported by the National Natural Science Foundation of China (52078286).

References

[1] X. Liu, Q. Fang, D. L. Zhang, and Z. J. Wang, "Behaviour of existing tunnel due to new tunnel construction below," *Computers and Geotechnics*, vol. 110, pp. 71–81, 2019.

[2] R. Z. Liang, T. D. Xia, Y. Hong, and F. Yu, "Effects of above-crossing tunneling on the existing shield tunnels," *Tunnelling and Underground Space Technology*, vol. 58, pp. 159–176, 2016.

[3] D. L. Jin, D. J. Yuan, S. Y. Liu, X. G. Li, and W. Luo, "Performance of existing subway tunnels undercrossed by four closely spaced shield tunnels," *Journal of Performance of Constructed Facilities*, vol. 33, no. 1, Article ID 04018099, 2019.

[4] C. W. W. Ng, K. Y. Fong, and H. L. Liu, "The effects of existing horseshoe-shaped tunnel sizes on circular crossing tunnel interactions: Three-dimensional numerical analyses," *Tunnelling and Underground Space Technology*, vol. 77, pp. 68–79, 2018.

[5] C. W. W. Ng, T. Boonyarak, and D. Mašín, "Three-dimensional centrifuge and numerical modeling of the interaction between perpendicularly crossing tunnels," *Canadian Geotechnical Journal*, vol. 50, no. 9, pp. 935–946, 2013.

[6] H. Mohamad, P. J. Bennett, K. Soga, R. J. Mair, and k. Bowers, "Behaviour of an old masonry tunnel due to tunnelling-induced ground settlement," *Géotechnique*, vol. 60, no. 12, pp. 927–938, 2010.

[7] H. P. Lai, H. W. Zheng, R. Chen, Z. Kang, and Y. Liu, "Settlement behaviors of existing tunnel caused by obliquely under-crossing shield tunneling in close proximity with small intersection angle," *Tunnelling and Underground Space Technology*, vol. 97, p. 103258, Article ID 103258, 2020.

[8] R. P. Chen, X. T. Lin, X. Kang et al., "Deformation and stress characteristics of existing twin tunnels induced by close-distance EPBS under-crossing," *Tunnelling and Underground Space Technology*, vol. 82, pp. 468–481, 2018.

[9] Z. Zhou, Y. Chen, Z. Z. Liu, and L. W. Miao, "Theoretical prediction model for deformations caused by construction of new tunnels undercrossing existing tunnels based on the equivalent layered method," *Computers and Geotechnics*, vol. 123, p. 103565, Article ID 103565, 2020.

[10] L. Andersen and C. J. C. Jones, "Coupled boundary and finite element analysis of vibration from railway tunnels-a comparison of two- and three-dimensional models," *Journal of Sound and Vibration*, vol. 293, no. 3-5, pp. 611–625, 2006.

[11] J. A. Forrest and H. E. M. Hunt, "A three-dimensional tunnel model for calculation of train-induced ground vibration," *Journal of Sound and Vibration*, vol. 294, no. 4-5, pp. 678–705, 2006.

[12] E. Celebi, "Three-dimensional modelling of train-track and sub-soil analysis for surface vibrations due to moving loads," *Applied Mathematics and Computation*, vol. 179, no. 1, pp. 209–230, 2006.

[13] M. F. M. Hussein and H. E. M. Hunt, "A numerical model for calculating vibration from a railway tunnel embedded in a full-space," *Journal of Sound and Vibration*, vol. 305, no. 3, pp. 401–431, 2007.

[14] S. Gupta, G. Degrande, and G. Lombaert, "Experimental validation of a numerical model for subway induced vibrations," *Journal of Sound and Vibration*, vol. 321, no. 3-5, pp. 786–812, 2009.

[15] H. H. Hung, G. H. Chen, and Y. B. Yang, "Effect of railway roughness on soil vibrations due to moving trains by 2.5D finite/infinite element approach," *Engineering Structures*, vol. 57, pp. 254–266, 2013.

[16] X. Bian, H. Jiang, C. Cheng, Y. M. Chen, R. P. Chen, and J. Q. Jiang, "Full-scale model testing on a ballastless high-speed railway under simulated train moving loads," *Soil Dynamics and Earthquake Engineering*, vol. 66, pp. 368–384, 2014.

[17] Y. Shan, S. Zhou, and Y. Shu, "Differential settlement and soil dynamic stress of a culvert-embankment transition zone due to an adjacent shield tunnel construction," *KSCE Journal of Civil Engineering*, vol. 22, no. 7, pp. 2325–2333, 2018.

[18] H. R. Nejati, M. Ahmadi, and H. Hashemolhosseini, "Numerical analysis of ground surface vibration induced by underground train movement," *Tunnelling and Underground Space Technology*, vol. 29, pp. 1–9, 2012.

[19] J. Ge, Y. Xu, and W. Cheng, "Key construction technology of shield tunneling crossing underneath a railway," *Infrastructure*, vol. 1, no. 1, p. 4, 2016.

[20] Y. Shan, S. H. Zhou, Q. M. Gong, and B. L. Wang, "Influence of shield tunnel construction beneath a railway on a culvert-embankment transition zone," in *Proceedings of the American Society of Civil Engineers Fifth International Conference on Transportation Engineering*, pp. 1001–1008, ASCE, Dailan, China, September 2015.

[21] Y. Shan, S. H. Zhou, Q. M. Gong, B. L. Wang, Y. Shu, and Z. G. Zhao, "Soil Dynamic stress of a Transition zone influenced by the shield Tunnel beneath a railroad," *Transportation Research Record: Journal of the Transportation Research Board*, vol. 2579, no. 1, pp. 40–47, 2016.

[22] C. J. C. Jones, D. J. Thompson, and M. Petyt, "A model for ground vibration from railway tunnels," *Proceedings of the Institution of Civil Engineers - Transport*, vol. 153, no. 2, pp. 121–129, 2002.

[23] W. Yang, M. F. M. Hussein, and A. M. Marshall, "Centrifuge and numerical modelling of ground-borne vibration from an underground tunnel," *Soil Dynamics and Earthquake Engineering*, vol. 51, pp. 23–34, 2013.

[24] Q. Huang, H. W. Huang, B. Ye, D. M. Zhang, L. L. Gu, and F. Zhang, "Dynamic response and long-term settlement of a metro tunnel in saturated clay due to moving train load," *Soils and Foundations*, vol. 57, no. 6, pp. 1059–1075, 2017.

[25] W. F. Anderson and A. J. Key, "Model testing of two-layer railway track ballast," *Journal of Geotechnical and Geoenvironmental Engineering*, vol. 126, no. 4, pp. 317–323, 2000.

[26] D. Negrut, R. Rampalli, G. Ottarsson, and A. Sajdak, "On an implementation of the Hilber-Hughes-Taylor method in the context of index 3 differential-algebraic equations of multibody dynamics (DETC2005-85096)," *Journal of Computational and Nonlinear Dynamics*, vol. 2, no. 1, pp. 73–85, 2007.

[27] P. Asnachinda, T. Pinkaew, and J. A. Laman, "Multiple vehicle axle load identification from continuous bridge bending moment response," *Engineering Structures*, vol. 30, no. 10, pp. 2800–2817, 2008.
[28] L. Fryba, *Vibration of solids and structure under Moving Loads*, Noordhoff International Publishing, Groningen, 1972.
[29] L. Yu and T. H. T. Chan, "Moving force identification based on the frequency-time domain method," *Journal of Sound and Vibration*, vol. 261, no. 2, pp. 329–349, 2003.
[30] T. H. Chan and D. B. Ashebo, "Theoretical study of moving force identification on continuous bridges," *Journal of Sound and Vibration*, vol. 295, no. 3-5, pp. 870–883, 2006.
[31] D. Cebon, *Hand Book of Vehicle-Road Interaction*, Sweets & Zeitlinger Publishers, 1999.
[32] J. B. Liu, Y. X. Du, X. L. Du, Z. Y. Wang, and J. Wu, "3D viscous-spring artificial boundary in time domain," *Earthquake Engineering and Engineering Vibration*, vol. 5, no. 1, pp. 93–102, 2006.
[33] M. M. Alhassan, T. Huff, and D. R. VandenBerge, "Effects of Rayleigh-Damping approach on the elastic and inelastic seismic performance of fixed-and flexible-base structural systems," *Practice Periodical on Structural Design and Construction*, vol. 26, no. 3, Article ID 04021021, 2021.
[34] M. Kavvadas, D. Litsas, I. Vazaios, and P. Fortsakis, "Development of a 3D finite element model for shield EPB tunnelling," *Tunnelling and Underground Space Technology*, vol. 65, pp. 22–34, 2017.
[35] A. Lambrughi, L. Medina Rodríguez, and R. Castellanza, "Development and validation of a 3D numerical model for TBM-EPB mechanised excavations," *Computers and Geotechnics*, vol. 40, pp. 97–113, 2012.
[36] D. P. Connolly, G. Kouroussis, P. K. Woodward, P. Alves Costa, O. Verlinden, and M. C. Forde, "Field testing and analysis of high speed rail vibrations," *Soil Dynamics and Earthquake Engineering*, vol. 67, pp. 102–118, 2014.
[37] Q. X. Yan, B. Li, P. Geng, C. Chen, C. He, and W. B. Yang, "Dynamic response of a double-lined shield tunnel to train impact loads," *Tunnelling and Underground Space Technology*, vol. 53, pp. 33–45, 2016.